



**Subject Areas:**

Computer modelling and simulation,  
Fluid mechanics

**Keywords:**

Micro-origami simulation, drop  
encapsulation, self-folding,  
fluid-structure interaction.

**Author for correspondence:**

Gregory Lecrivain

e-mail: [g@lecrivain.hzdr.de](mailto:g@lecrivain.hzdr.de)

# Self-folding of two-dimensional thin templates into pyramidal micro-structures by a liquid drop - a numerical model

Gregory Lecrivain<sup>1</sup>, Pierre Lorenz<sup>2</sup>, Klaus Zimmer<sup>2</sup> and Uwe Hampel<sup>3</sup>

<sup>1</sup>Helmholtz-Zentrum Dresden-Rossendorf, Institut für Fluidodynamik, Bautzner Landstraße 400, 01328 Dresden, Germany

<sup>2</sup>Leibniz-Institut für Oberflächenmodifizierung, Permoserstraße 15, 04315 Leipzig, Germany

<sup>3</sup>Technische Universität Dresden, Institut für Energietechnik, Professur für Bildgebende Messverfahren für die Energie- und Verfahrenstechnik, Dresden, Germany

We present a numerical framework bringing together a structural and a surface-energy minimization model to compute nano- and micro-origami self-folding processes, that are three-dimensional in nature. A liquid drop, initially at rest on the template, triggers the spontaneous folding and deforms dynamically with the template. As application, the self-folding of thin two-dimensional templates into pyramidal micro-structures is simulated. Each template is composed of a fixed regular base connected to rigid triangular side panels by two elastic hinges. We presently determine the condition, at which the transition from partial to full drop encapsulation occurs. The present model makes use of phase fields to numerically represent the drop and the template. This allows to a) develop an efficient computational method, which incorporates time-derivative terms and b) study three-dimensional complex self-folding processes.

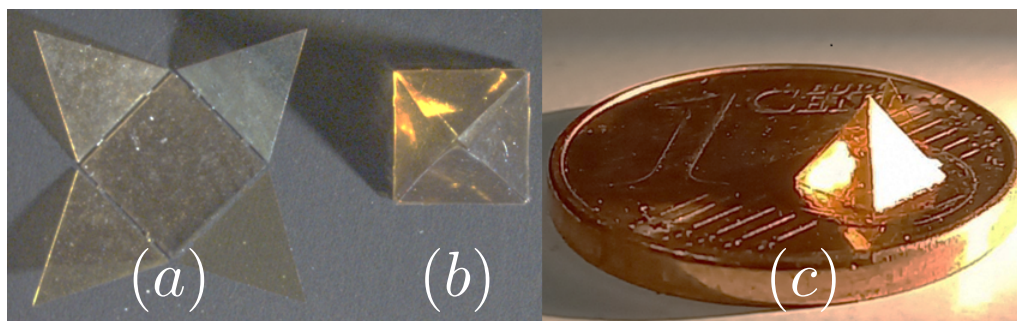


**Figure 1.** Using a liquid drop, the unfolded two-dimensional template (a), called a structural net, spontaneously turns into a pyramidal micro-structure (b-c). Hinges, connecting the base to each triangular side panel, deform during the folding. Eventually, the drop is fully encapsulated by the structural net. The experiment was performed for illustration purposes.

## 1. Introduction

### (a) General context

Capillary-induced nano and micro-origami are processes, by which surface tension spontaneously folds a thin planar template into a hollow three-dimensional structure [1–5]. In nature, petaled flowers have developed self-folding properties, that are solely triggered by surface tension [6]. In nano and micro-engineering involving thin film planar technology [7–10], three-dimensional structures have been produced by depositing a liquid drop onto thin and foldable two-dimensional polymer templates. Figure 1 illustrates a pyramidal microstructure, that we obtained by placing a drop onto a specific thin planar template, specifically referred to as structural “net” in the technical literature [11–13]. Elastic hinges, connecting each side panel of the net to the rectangular base, hold the template together. The liquid drop, by minimizing its contact surface to the ambient air, triggers large deformation of the hinges and hence the folding. By appropriately tailoring the structural net, the final folded structure remains three-dimensional after the drop fully evaporates [14]. Inspired by that, micro-origami has found application in biomedicine, for example, in the selective encapsulation of cells and bacteria by functionalizing the surfaces of a foldable template [15–17].

### (b) State-of-the-art and current limitations

The simulation of self-encapsulation, that is the spontaneous encapsulation of a liquid drop by a thin and deformable two-dimensional template, is challenging. Strong structural deformation, moving contact line, drop affinity to the template along with water evaporation should ideally be taken into account. A number of models have been suggested in the past. Patra et al. [18] used molecular dynamics to simulate the self-folding of a graphene petal-like structural net by a nano-drop. In their three-dimensional simulation, thousands of water molecules were used to discretize the nano-drop. Liu et. al [19] also used three-dimensional molecular dynamics to investigate the self-folding of various graphene templates. In their work, the initial two-dimensional templates were rectangular, circular and triangular thin sheets. Further three-dimensional methods exist. One of them is based on the Surface Evolver [20]. Leong et al. [21] used it to simulate the self-folding of structural nets into micro-cubes with a quasi-static assumption. The structural nets were made of thin square panels connected to one another by deformable hinges. In their work, the Surface Evolver was used to iteratively re-distribute the nodes of the drop surface by minimizing its surface energy. Similarly, in [22,23], the authors investigated the fabrication of

five-faced micro-cubes. By deliberately omitting the top surface of the micro-cube, the volume of water could be greater than that of the closed micro-cube. In their work, a variational approach was used. The total energy, that is the sum of a bending energy associated with the hinge deformation and an interfacial energy associated with the drop deformation, was minimized. To model the hinge, a dimensionless parameter was introduced. It characterized the ratio of the reference bending force to the surface tension force. Further models based on the variational approach have been suggested for self-folding simulations [24,25], yet they are mostly limited to two-dimensional simulations. Brubaker et al. [26] are one of the few groups to have attempted to simulate the three-dimensional self-folding with a variational approach. Their three-dimensional extension, described as highly challenging by the authors, was however only valid for small deformations and could not accurately capture the full encapsulation of the drop. Finally, Neukirch et al. [27] derived equilibrium solutions for a two-dimensional drop resting on an elastic beam. Self-encapsulation by an elastic rod was also studied experimentally and numerically in [28].

To conclude, three-dimensional self-folding simulations have been performed using molecular dynamics with van der Waals and Coulomb interactions. Despite the excellent versatility of molecular dynamics in defining the initial template shape, such simulations are still computationally expensive and limited in atom number [29]. Liu et al. [19], for instance, used about 20,000 water molecules to model a nano-drop. Three-dimensional extensions based on energy minimization are faster, because they consider both the drop and the template as continuum. Yet, most three-dimensional variational continuum models are either limited to small deformations or reductive. It is often assumed, that the drop takes the shape of a spherical cap throughout the folding process [26,30]. More complex continuum variational models, which describe both the drop and the template deformation simultaneously, are usually two-dimensional [27].

### (c) Objectives

An alternative method is here proposed to simulate the three-dimensional self-folding of a structural net composed of thin panels connected to one another by elastic hinges. As academic application, star-like structural nets are chosen because they are reminiscent of those presented in [21–23]. In their final states, the folded micro-structures take pyramidal shapes. Our method, based on a continuum Allen-Cahn description [31], is different from those currently found in the literature. In particular, phase field models, to which the Allen-Cahn model also belongs, are a class of efficient computational methods that allow the study of complex three-dimensional systems. With our method, the simultaneous folding of the structural net along with the drop deformation are possible in just two hours on a personal computer.

This manuscript is arranged as follows. In the methods, we first begin by describing the hinge model. Second, we describe the drop deformation model based on the minimization of a free energy. The dynamic coupling between the two models is then addressed by providing a numerical description for the calculation of the surface tension force. In the results, we showcase the self-folding of the star-like structural nets into micro-pyramids and determine the necessary condition triggering a full encapsulation of the drop, as experimentally illustrated in Figure 1b-c.

## 2. Methods

At simulation start, the structural nets are unfolded pyramidal micro-structures with a regular polygonal base composed of  $N = 3, 4, 5, 6$  and  $7$  triangular side panels. A greater number of side panels is possible. The base is fixed and connects to each side panel by two deformable hinges. Figure 2 shows some selected structural nets, on which the drop initially rests. With a zero hinge length, the volume  $\mathcal{V} = \mathcal{A}h/3$  of each pyramid is identical. The base area  $\mathcal{A}$  and the height  $h$  of each pyramid are hence identical too and are set to  $\mathcal{V} = V_d$  and  $h = 4.1R_d$ , where  $V_d$  is the drop volume and  $R_d$  the equivalent drop radius. Considering a hemisphere as equivalent drop

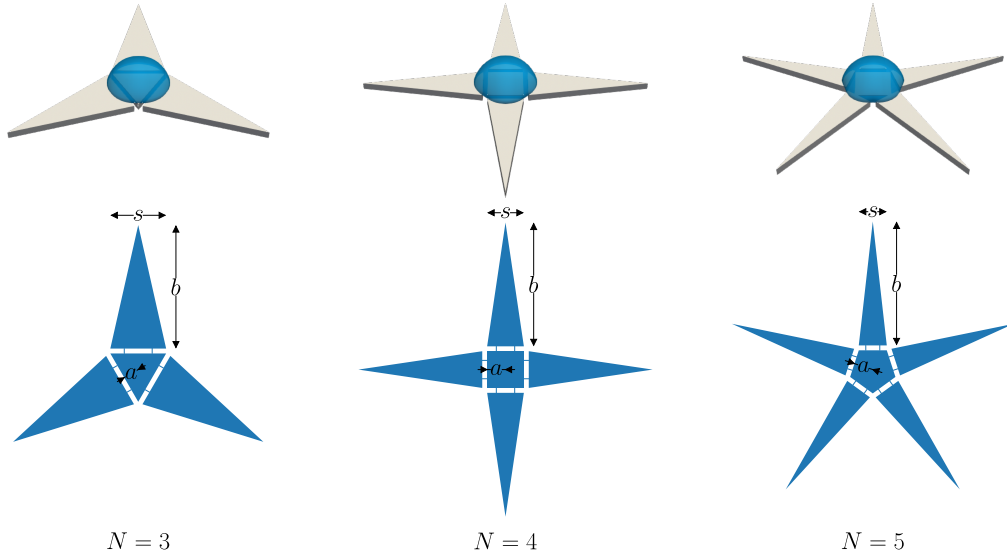


**Figure 2.** Unfolded pyramidal micro-structures, or structural nets.  $a$  is the apothem of the base panel.  $s$  and  $b$  are side length and height of each triangular panel. Each triangular side panel is connected to the base by two deformable hinges. Using the marching cubes [33], the drop is conveniently represented by a three-dimensional surface mesh.

geometry, the equivalent radius is given by  $V_d = 2/3\pi R_d^3$ . With  $a$  the apothem of the polygonal base,  $s$  and  $b$  the base and height of each triangular side panel, the length parameters of each unfolded structural net are given by

$$a^2 = \frac{A}{N} \cot\left(\frac{\pi}{N}\right), \quad (2.1)$$

$$s^2 = 4 \frac{A}{N} \tan\left(\frac{\pi}{N}\right), \quad (2.2)$$

$$b^2 = h^2 + a^2. \quad (2.3)$$

The shortest distance separating the base to each side panel, which is here the hinge length, is set to  $\ell/R_d = 0.164$ . In the simulation, the base and side panels are arbitrarily thin prisms represented by a triangulated surface mesh. In accordance with computer graphics [32], each surface mesh is described by an array of vertices and triangular faces. We note, that the panel thickness in the structural net, even though it later appears in Equation 2.16 to adequately model the drop affinity to the material, is here neglected. Hence, the panels are assumed to have negligible mass and inertia compared to the drop.

### (a) Hinges

To simulate the hinge deformation, the cohesive beam model [34] derived analytically from the Euler-Bernoulli beam theory [35] is here used. Because the hinge model is already presented in the author's previous work [36], we focus here on its most salient features. Each hinge is discretized into a chain of  $n_b$  spherical beads with identical radii  $r_b$ . As illustrated in Figure 3, the first bead with index  $i = 1$  is connected to the base and the last one to the side panel. The trajectory of each

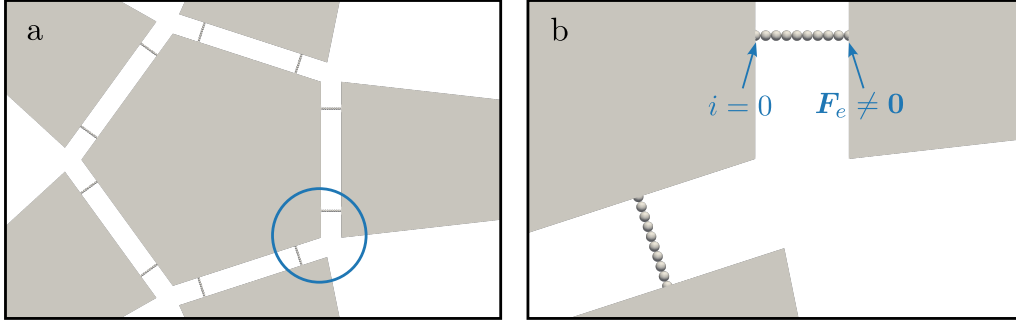


**Figure 3.** Each hinge is decomposed into  $n_b = 10$  spherical beads. The first bead, associated with the index  $i = 1$ , is fixed to the base. The external force only acts on the last bead, to which the triangular side panel is attached.

bead is computed independently as

$$\frac{d\mathbf{X}_i}{dt} = \mathbf{U}_i, \quad (2.4)$$

$$\frac{d\mathbf{Q}_i}{dt} = \frac{1}{2} \mathbf{A}_i \cdot \mathbf{Q}_i, \quad (2.5)$$

where  $\mathbf{X}_i$  is the position of  $i$ -th bead centre of mass,  $\mathbf{Q}_i = (Q_s \ Q_x \ Q_y \ Q_z)_i^\top$  the quaternion associated with the angular position of the bead,  $(Q_s)_i$  and  $(Q_x \ Q_y \ Q_z)_i^\top$  the scalar and vector parts of the quaternion,  $\mathbf{U}_i$  and  $\mathbf{\Omega}_i = (\Omega_x \ \Omega_y \ \Omega_z)_i^\top$  the translational and rotational velocities and  $\mathbf{A}_i$  a  $4 \times 4$  orthogonal matrix given by

$$\mathbf{A}_i = \begin{pmatrix} 0 & -\Omega_x & -\Omega_y & -\Omega_z \\ \Omega_x & 0 & -\Omega_z & \Omega_y \\ \Omega_y & \Omega_z & 0 & -\Omega_x \\ \Omega_z & -\Omega_y & \Omega_x & 0 \end{pmatrix}_i. \quad (2.6)$$

The dot operator in Equation 2.5 denotes the product  $A_{ij}Q_j$  used in the conventional ij-matrix notation. Each bead interacts with its next consecutive neighbor by a virtual beam (see Figure 4). At each extremity of the virtual beam, a structural force  $\mathbf{F}_b$  and torque  $\mathbf{T}_b$  are exerted on the  $i$ -th bead and its next neighbor, the  $j$ -th bead, where  $j = i + 1$ . With these structural forces yet to be formulated, the velocities of each bead are given by

$$m_b \left( \frac{d\mathbf{U}_i}{dt} + \frac{\mathbf{U}_i}{\tau_b} \right) = (\mathbf{F}_b)_i + \mathbf{F}_e, \quad (2.7)$$

$$\mathbf{I}_b \cdot \left( \frac{d\mathbf{\Omega}_i}{dt} + \frac{\mathbf{\Omega}_i}{\tau_b} \right) = (\mathbf{T}_b)_i + \mathbf{T}_e, \quad (2.8)$$

where  $m_b$  is the bead mass,  $\mathbf{I}_b$  a diagonal matrix whose components are the bead inertia moments,  $\tau_b$  a response time accounting for material damping [37],  $\mathbf{F}_e$  and  $\mathbf{T}_e$  external force and torque associated with the surface tension. In this work,  $\mathbf{F}_e$  and  $\mathbf{T}_e$  only act on the last bead of the hinge. In the beam model, the structural forces  $(\mathbf{F}_b)_i$  and  $(\mathbf{F}_b)_j$  are conveniently expressed in the local beam frame  $(\mathbf{X}_i \mathbf{e}_{x'} \mathbf{e}_{y'} \mathbf{e}_{z'})$ . The unit vector defined in the axial beam direction is given by  $\mathbf{e}_{x'} = (\mathbf{X}_j - \mathbf{X}_i)/|\mathbf{X}_j - \mathbf{X}_i|$ . The corresponding component of the structural force acting on the  $i$ -th and  $j$ -th beads are given by

$$(\mathbf{F}_b \cdot \mathbf{e}_{x'})_i = \frac{\pi E r_b}{2} \left( |\mathbf{X}_j - \mathbf{X}_i| - 2r_b \right), \quad (2.9)$$

$$(\mathbf{F}_b \cdot \mathbf{e}_{x'})_j = -(\mathbf{F}_b \cdot \mathbf{e}_{x'})_i, \quad (2.10)$$

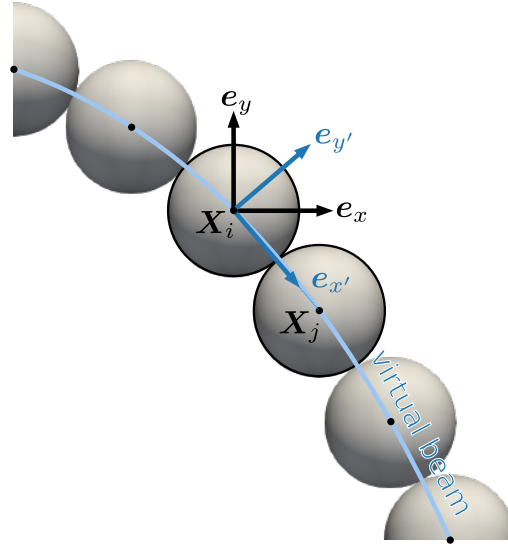


**Figure 4.** A bead interacts with its direct neighbors via structural forces derived from the elastica theory. The structural forces are conveniently expressed in the local beam frame  $(\mathbf{X}_i \mathbf{e}_{x'} \mathbf{e}_{y'} \mathbf{e}_{z'})$ .

where  $E$  is the Young modulus with respect to the hinge material. The other two force components acting in the tangential beam directions along with the torques are formulated in [36], whereby a similar notation has purposely been used here. The bead position and quaternion are integrated in time via an explicit first-order forward method and velocities via an explicit second-order Adams-Bashforth method. We define the reference structural force associated with the hinge as

$$F_s = \frac{EI}{\ell^2}, \quad (2.11)$$

where  $I = \pi r_b^4/4$  is the area moment of inertia and  $\ell = 2r_b(n_b - 1)$  the hinge length.

The above hinge model could well be replaced with an analytical model for large deformation [38,39]. The reason behind the chain decomposition into beads is twofold. First, the bead model was already available and implemented. Second, our original intention was to model the drop affinity to the hinge as well, which we eventually abandoned because the beads turned out to be a lot smaller than the panels of the structural net.

## (b) Drop

The liquid drop, the ambient gas and the structural net are replaced with continuous concentration fields  $\phi_\ell(\mathbf{x}, t)$ ,  $\phi_g(\mathbf{x}, t)$  and  $\phi_s(\mathbf{x}, t)$ , where  $\mathbf{x} = (x y z)^\top$  is a point in space and  $t$  the time. The hinge is here left out because it is spatially too small to be considered a field. As one moves from the inner to the outer phase region, each concentration field smoothly varies from unity to zero over an interfacial width  $\xi$ . The drop shape is a-priori unknown. Hence, a modified Allen-Cahn model [31], that relies on the minimization of a free energy  $E(\phi, \nabla\phi)$  following the Ginzburg–Landau theory [40], is here employed. Dropping the subscript associated with the liquid for better readability, that is  $\phi = \phi_\ell$ , the spacial and temporal evolution of the liquid concentration is obtained by solving

$$\frac{\partial \phi}{\partial t} + \mathbf{u} \cdot \nabla \phi = -\frac{1}{\tau_d} \frac{\delta \tilde{E}}{\delta \phi}, \quad (2.12)$$

where  $\mathbf{u}$  is an Eulerian velocity field associated with the folding of the structural net,  $\tau_d$  a response time associated with the mobility of the drop,  $\tilde{E} = E/E_0$  the free energy in its non-dimensional form,  $E_0 = k_B T_0/L_0^3$  the reference energy,  $k_B$  the Boltzmann constant,  $T_0$  the temperature, and  $L_0$  a reference length [41]. The advection term  $\mathbf{u} \cdot \nabla \phi$  on the left-hand side of Equation 2.12 contributes to a change in the drop shape caused by the displacement of each side panel, while the right-hand side term strives for an energetically stable drop shape. The functional derivative of the free energy is suggested as

$$\frac{\delta \tilde{E}}{\delta \phi} = f_b(\phi) - \xi^2 \nabla^2 \phi + f_\ell(\phi, \phi_g, \phi_s) + f_w(\phi, \phi_s, \gamma), \quad (2.13)$$

where  $f_b$  is a bulk term,  $-\xi^2 \nabla^2 \phi$  an interfacial term addressing the smooth transition from unity to zero across the interface,  $f_\ell$  a Lagrangian multiplier,  $f_w$  a wall correction term accounting for the drop affinity to the template and  $\gamma$  the contact angle. The bulk term, derived from a double-well potential having two local minima located at  $\phi = 0$  and  $\phi = 1$ , is given by

$$f_b = 4\phi(\phi - 1)(\phi - \phi_c), \quad (2.14)$$

where  $\phi_c = 1/2 + \beta(V_t/V_d - 1)$  is a corrected term maintaining the constant drop volume  $V_d$  [42, 43],  $\alpha > 0$  a growth rate,  $V_t = \int \phi^2 dv$  the drop volume at time  $t$  and  $dv$  an infinitesimally small volume element. The Lagrangian multiplier is given by  $f_\ell = -\phi\phi_g\phi_s$ , with  $\phi_g = 1 - \phi_s - \phi$  owing to mass conservation. In short,  $f_\ell$  ensures that all functional derivatives related to the present ternary system are equal to zero at equilibrium, that is  $\delta \tilde{E}/\delta \phi = \delta \tilde{E}/\delta \phi_g = \delta \tilde{E}/\delta \phi_s = 0$ . For more information about the Lagrangian multiplier, we refer the reader to the original literature [44,45]. The wall contribution, taken from [46], is given by

$$f_w = \phi(\phi - 1)|\mathbf{n}| \cos(\gamma) - \xi^2 \nabla \phi \cdot \nabla \phi_s, \quad (2.15)$$

with  $\mathbf{n} = \xi \nabla \phi_s$ , the wall-normal vector field. Because the free energy  $E$  never appears in the implementation, its formulation has deliberately been omitted. Only its functional derivative, appearing in Equation 2.12, is here relevant. The individual concentration field associated with each surface mesh, or prism, representing the structural net is given by

$$\phi_p = \frac{1}{2} \left[ 1 - \tanh \left( \frac{d}{\xi} \right) \right], \quad (2.16)$$

where  $d(\mathbf{x})$  is the shortest signed distance from the point  $\mathbf{x}$  to the sharp prism boundary. The distance  $d$  is calculated using the pseudo-normal method [47], which works well for closed, non-self-intersecting and manifold surface meshes, as is the case here. From this, the total concentration field associated with the structural net ensues as

$$\phi_s = \sum \phi_p. \quad (2.17)$$

For the special case, in which the liquid only co-exists with the gas, that is  $\phi_s = 0$ , Equation 2.13 reduces to  $\delta \tilde{E}/\delta \phi = 4\phi(\phi - 1)(\phi - 1/2) - \xi^2 \nabla^2 \phi$ . In a one dimensional space, it can be analytically shown, that the solution to  $\delta \tilde{E}/\delta \phi = 0$  is  $\phi(x) = 1/2 - \tanh(x/\xi)/2$  [48], which exactly corresponds to the mathematical expression in Equation 2.16. Equation 2.12 is integrated in time using an explicit first-order forward method. Its advection term  $\mathbf{u} \cdot \nabla \phi$  is discretized in space using a first-order upwind scheme. The Laplacian operator ( $\nabla^2$ ) in Equation 2.13 and the gradient operators ( $\nabla$ ) in Equation 2.15 are discretized via second order schemes. The reference surface tension force is hereafter given by

$$F_c = \sigma R_d, \quad (2.18)$$

where  $R_d$  is the equivalent drop radius previously defined and  $\sigma$  the surface tension.

## (c) Coupling

The model is closed when the surface tension force  $\mathbf{F}_e$  and torque  $\mathbf{T}_e$  acting on the last bead of each hinge are known. These act as external term in Equations 2.7-2.8. There exist various



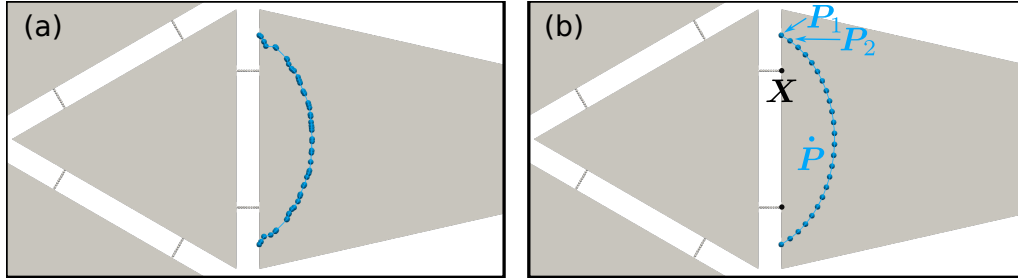


**Figure 5.** Original (a) and smoothed (b) three-phase contact line obtained by intersecting a side panel of the structural net with the drop.  $L_c = \sum |\mathbf{P}_{i+1} - \mathbf{P}_i|$  is the length of the three phase contact line on one side panel.

methods to estimate  $\mathbf{F}_e$  and  $\mathbf{T}_e$ . We cite for instance the continuous force model [49,50]. We here adopt another strategy based on intersecting the sharp interface of the drop with the structural net. First, the marching cubes method [33] is used to determine a tessellated surface mesh of the drop from the smooth concentration field  $\phi$ . We are free to choose any iso-value for  $\phi$ . A natural candidate would be  $\phi = 0.5$ . Our simulations have however shown, that the drop iso-surface does not always intersect with the triangular side panel for high contact angle, typically  $\gamma > 120^\circ$ . A small distance, typically one grid spacing  $\delta x$ , may separate the drop iso-surface from the surface mesh representing the triangular side panel. A simple, yet effective work around, consists in selecting a slightly lower iso-value, in this case,  $\phi = 0.4$ . Second, the geometrical intersection between the surface meshes representing the drop and the top surface of each triangular side panel are performed, resulting in a first set of polylines representing the three-phase contact lines. Because of the tessellation, the contact line is not smooth. Therefore, a new polyline  $\{\mathbf{P}_i\}$  is determined by approximating it with a spline [51]. Figure 5 shows the smooth redistribution of the points forming the three-phase contact line on the side panel. The calculation of the wall-normal surface tension force is relatively straightforward. It is given by

$$\mathbf{F}_e = \frac{\sigma}{2} L_c \sin(\gamma) \mathbf{n}, \quad (2.19)$$

where  $L_c$  is the length of the three-phase contact line given by

$$L_c = \sum |\mathbf{P}_{i+1} - \mathbf{P}_i|. \quad (2.20)$$

Accordingly, the external torque is given by

$$\mathbf{T}_e = \mathbf{F}_e \times (\mathbf{P} - \mathbf{X}), \quad (2.21)$$

where  $\mathbf{P}$  is the barycentre of the three-phase contact line  $\{\mathbf{P}_i\}$  and  $\mathbf{X} = (\mathbf{X})_{n_b}$  the position of the last bead, whose index has been dropped. We recall that each triangular panel is pinned to the last bead of the hinge, whose position  $\mathbf{X}$  and velocities  $\mathbf{U}$  and  $\mathbf{\Omega}$  are known. The velocity of each mobile panel hence converts to an individual Eulerian field  $\mathbf{u}_p = \mathbf{U} + \mathbf{\Omega} \times \mathbf{r}$ , where  $\mathbf{r} = \mathbf{x} - \mathbf{X}$ . Finally, the total velocity in Equation 2.12 is given by  $\mathbf{u} = \sum \phi_p \mathbf{u}_p$ .

For the implementation of the model, ingredients from various independent sources were used. To solve the advection Equation 2.12, the “PETSc” library [52], which comes with a series of data structures and routines for solving partial differential equations on high performance computer, is used. For operations on the tessellated objects, that are the calculation of the shorted distance to the wall (Equation 2.16) and the determination of the three-phase contact line by intersecting two tessellated mesh surfaces, the “libigl” library [32] is used. For smoothing the three-phase contact line, the “fitpack” library [53] is used. The presented method has been implemented using the Message Passing Interface for enhanced performance. In an engineering context, the model, as will be shown later, performs well and shows a relatively good performance



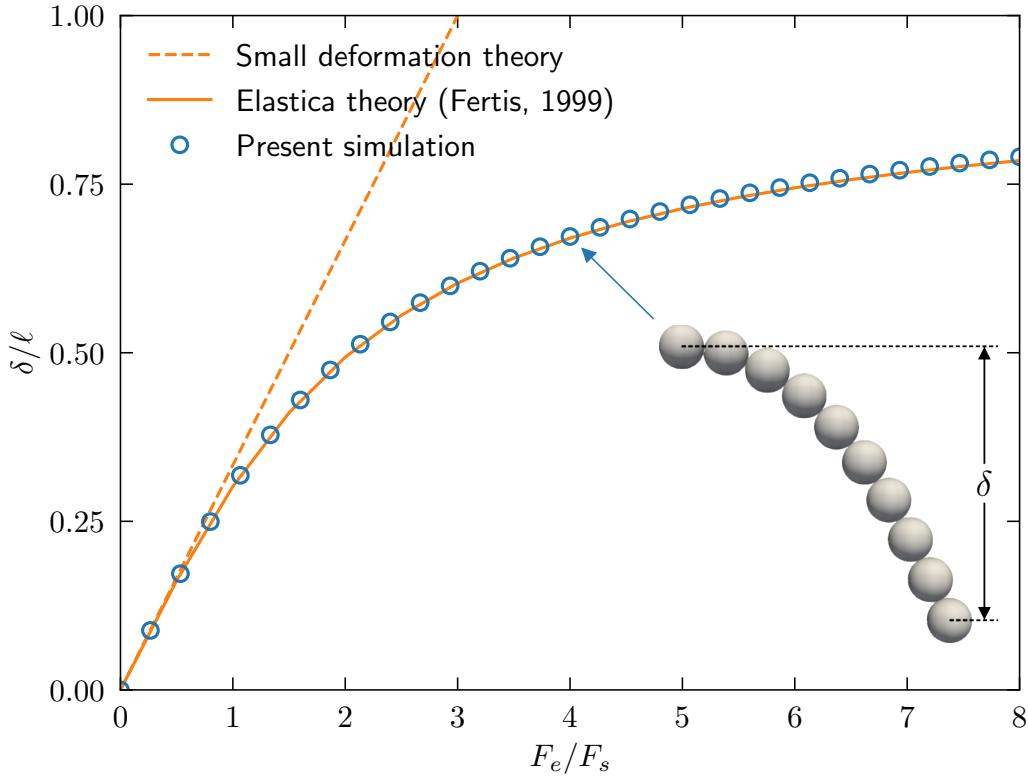


**Figure 6.** Vertical deflection  $\delta$  of hinge composed of ten beads against external load  $F_e$ . The denominator  $F_s$  in the abscissa is the reference structural force.  $\ell$  is the hinge length.

in terms of accuracy and computational time. The source code, which we documented, along with some of the raw data presented in the following have been made available [54].

### 3. Results

#### (a) Validation

First, the hinge model is validated. A hinge, composed of  $n_b = 10$  beads, is initially set in horizontal position and has its left extremity fixed. The position and velocity of the first bead is zero, that is  $\mathbf{X}_0 = \mathbf{0}$ ,  $\mathbf{U}_0 = \mathbf{0}$  and  $\mathbf{\Omega}_0 = \mathbf{0}$ . On the last bead, that is the right extremity of the hinge, an external force pointing downwards acts as  $\mathbf{F}_e = -F_e \mathbf{e}_y$ . The vertical deflection  $\delta$ , obtained after an equilibrium state is reached, is calculated at the hinge extremity. Figure 6 shows the deflection  $\delta$  as a function of the external load  $F_e$ , that we normalize with the reference structural force given in Equation 2.11. In the small-deflection region, which we define for  $F_e/F_s < 1$  based on the results, the vertical deflection increases linearly with the external load as

$$\frac{\delta}{\ell} = \frac{F_e}{3F_s}. \quad (3.1)$$

The analytical solution related to the large-deflection is provided in [35]. With a number of beads set to ten, the match in terms of bending between the simulation data and the theory is excellent for both the small and large structural deformations.

Second, we perform a mesh independence study for the validation of the three-phase contact line model. To this end, a drop is initially placed on the top surface of a rectangular thin template.

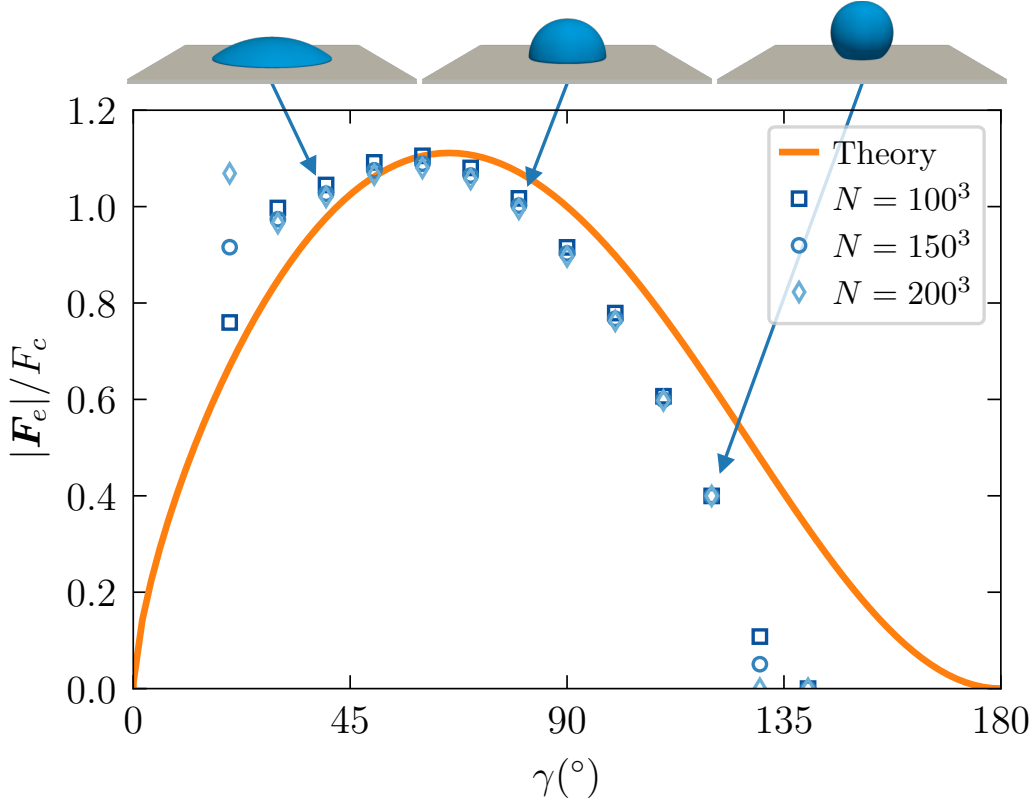


**Figure 7.** Surface tension force  $|F_e|$  acting on a flat template against contact angle  $\gamma$ . The reference capillary force is  $F_c = \sigma R_d$ , where  $R_d$  is the radius of the hemisphere obtained for  $\gamma = 90^\circ$ .

The mobile panels along with the hinges are here left out. The drop is initialized to a hemisphere with volume  $V_d$ . The contact angle,  $\gamma$ , is varied from  $20^\circ$  to  $140^\circ$ . The simulations are performed in a cubic domain discretized into  $100^3$ ,  $150^3$  and  $200^3$  grid points. The interfacial thickness in Equation 2.16 is hence gradually decreased from  $\xi$  to  $\xi/2$ , to  $\xi/3$ . Figure 7 shows the magnitude of the surface tension force  $F_e$ , calculated along the three-phase contact line using Equation 2.19, against the contact angle. The orange line corresponds to the theoretical solution, which assumes, that the drop at equilibrium takes the shape of a spherical cap [55,56]. In the intermediate region,  $30^\circ < \gamma < 120^\circ$ , the agreement between simulation and theory is relatively good. With a contact angle lower than  $\gamma < 20^\circ$ , full wetting occurs. The drop flattens and, in many cases, reaches the template boundaries. Under such circumstances, it becomes nearly impossible to determine the contact angle. That is one reason why the simulation blue points on the far left in Figure 7 may significantly deviate from the theoretical line. Beyond, that is in the region where strong to extreme dewetting occurs, deviation is also observed. In this upper interval, the three-phase contact line is generally short. Any small error in intersecting the drop iso-surface with the thin template results in relatively strong deviations. The increasing errors with decreased length of the three-phase contact line is reflected in Figure 7. For  $\gamma > 135^\circ$ , full dewetting occurs. A thin cushion with a height of about one unit grid spacing  $\delta x$  forms between the drop and the flat plate. For this reason, A contact line can not be determined. In all following simulations, we choose a cubic Eulerian domain made of  $150^3$  nodes and set the interfacial width equal to the one grid size element, that is  $\xi = \delta x$ .

Third, we compare the equilibrium three-phase contact line on a partly folded structural net to a semi-analytical solution. Because the structural net is here fixed, only Equation 2.12 with  $\mathbf{u} = \mathbf{0}$  is solved. We set the number of side panels to  $N = 4$ , the contact angle to  $\theta = 70^\circ$  and the folding angle to  $\alpha = 30^\circ$ . More information about the folding angle is provided later on in Section 3(c). For now, it is sufficient to know, that the structural net is partially folded and does not change with time. The hinges are left out, that is  $\ell = 0$ . Figure 8b shows the simulated drop at equilibrium. A comparative theoretical solution cannot be easily determined, we therefore resort to a semi-analytical model, in which the upper surface of the drop is represented by a spherical cap with radius  $R_c$  and centre-of-mass altitude  $h_c$ . The subscript “c” stands for “cap”. In this semi-analytical model, the lower drop surface not in contact with the structural net is made of  $N$  flat planes. As shown in Figure 8a, each plane passes through the nearest long edges of two side panels.  $R_c$  and  $h_c$  are a-priori unknown. We therefore simultaneously solve the equations  $V_c(R_c, h_c) = V_d$  and  $\theta_c(R_c, h_c) = \theta$  given the drop volume  $V_d$  and the contact angle  $\theta$ . Here,  $V_c$  is the semi-analytical drop volume calculated with a volume mesh generator [57] and  $\theta_c$  the contact angle determined analytically by arithmetic means. The description of the optimization technique used to simultaneously solve the pair of equations ( $V_c = V_d, \theta_c = \theta$ ) goes well beyond the scope of this work. If interested, the reader can consult the algorithm provided in [54]. Figure 8c shows the mean distance  $\Delta$  between the simulated contact line and its semi-analytical counterpart as a function of the drop volume, which varies from  $V_d/V = 0.5$  to 1.6. We recall that  $V$  is the volume of the folded pyramidal micro-structure. Prior to calculating the mean distance  $\Delta$ , each polyline represented the three-phase contact line is resampled into  $n = 100$  points. The schematics in Figure 8c illustrates the calculation of distance  $\Delta$ . For  $V_d/V = 1$ , which is of relevance in the following analysis, we observe a deviation from the semi-analytical solution of less than  $\Delta/s < 4\%$ . In Figure 8d, the semi-analytical three-phase contact line (orange curve) is overlaid with the simulated one (blue) for three selected drop volumes denoted by the letters  $i, j$  and  $k$ . Also here, a qualitatively good agreement between the two curves is observed.

## (b) Non-dimensionalization

Below the submillimetric scale, the surface tension force prevails by several orders of magnitude over the buoyancy and hydrostatic forces [27]. These contributions can hence be safely neglected. The key parameter in this study is the elasto-capillary number, defined as the ratio of the reference surface tension force to the reference structural force. It is here given by

$$Ec = \frac{F_c}{F_s}. \quad (3.2)$$

Typical values for  $Ec$  can be derived from previous experimental scenarios on self-folding. Van Honschoten et al. [22] fabricated micro-cube with an edge length set to about  $50 \mu\text{m}$ , which converts to an approximate drop radius  $R_d = 31 \mu\text{m}$ . The hinge thickness, which we take here as the bead radius, was  $r_b = 1 \mu\text{m}$ . The Young modulus of the material was  $E = 260 \text{ GPa}$ . The surface tension between air and water, taken from literature, was  $\sigma = 0.073 \text{ N/m}$ . The hinge length was varied from  $\ell = 2$  to  $10 \mu\text{m}$ . For the shortest hinge, respectively the longest, we find  $Ec = 0.44$  and  $11.08$ . In our recent experimental work [10], we also investigated experimentally the self-folding of a structural net into a milli-cube filled with water. The edge length of the cube was  $3 \text{ mm}$ , which converts to a drop radius  $R_d = 1.86 \text{ mm}$ . The length of the hinge was about  $\ell = 100 \mu\text{m}$  and the Young modulus of the material  $E = 0.27 \text{ GPa}$ . Self-folding occurred for a hinge thickness, which we also take as the bead radius, ranging from about  $r_b = 10$  down to  $5 \mu\text{m}$ . This results in an elasto-capillary number equal to  $Ec = 0.71$  and  $11.30$ , respectively. Based on the above two references, it is fair to assume an elasto-capillary number in the typical experimental range  $0.1 < Ec < 10$ . As will be seen in the next subsection, this range corresponds to that used in our simulations.

It is interesting to briefly discuss the non-dimensionalization of the equations using, among others, the elasto-capillary number. Let us first focus on the hinge Equation 2.9, which we divide

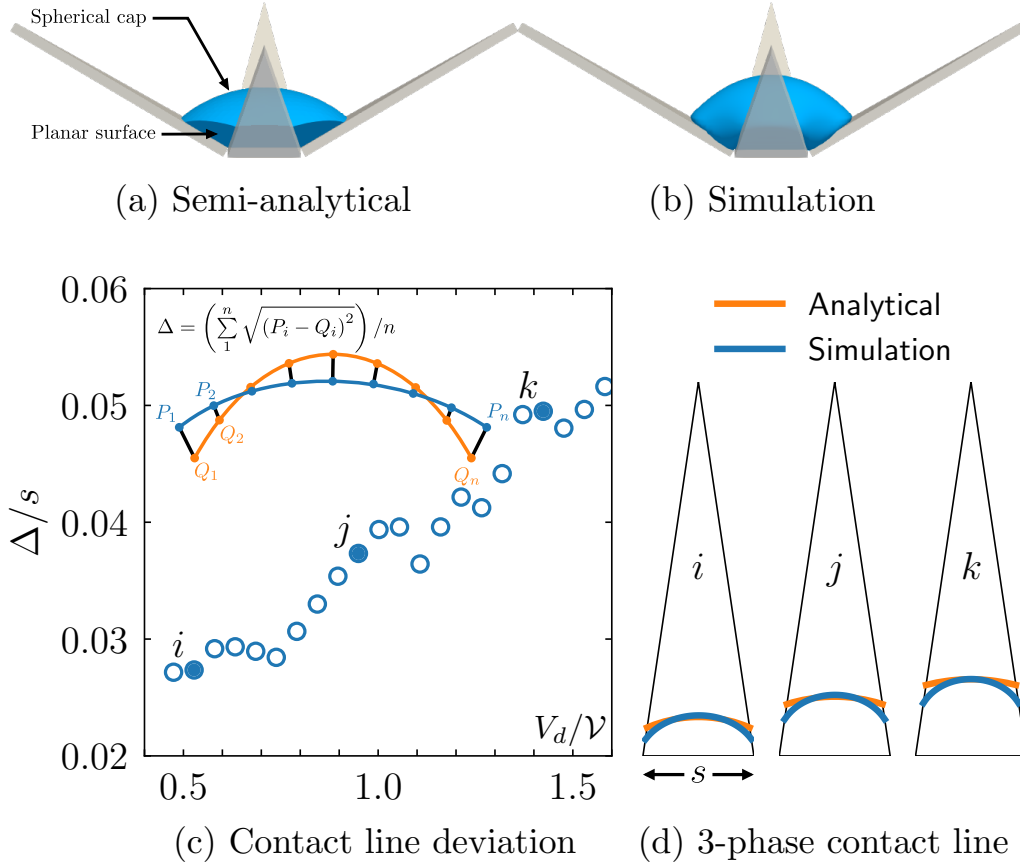


**Figure 8.** (a) Drop shape obtained with the semi-analytical method. (b) Simulated drop shape in equilibrium obtained by solving Equation 2.12. (c) Mean distance ( $\Delta$ ) from the simulated three-phase contact line to the semi-analytical solution. (d) Semi-analytical and simulated three-phase contact lines for selected volume  $V_d/V = 0.53, 0.95$  and  $1.42$ . The folding angle is set to  $\alpha = 30^\circ$  and the contact angle to  $\theta = 70^\circ$ .  $V_d$  is the volume of the drop and  $V$  that of the fully folded pyramid.

on each side by the reference structural force  $F_s$  earlier defined. For the sake of simplicity, the damping term is left out. After simplification, we obtain for the last virtual beam

$$K \left( \tilde{m} \frac{d\tilde{U}}{d\tilde{t}} \right) = 16(n_b - 1)^2 \left( \frac{|\mathbf{X}_j - \mathbf{X}_i|}{2r_b} - 1 \right) + \frac{L_c}{R_d} \sin(\gamma) Ec, \quad (3.3)$$

where  $K = \rho_0 U_0^2 L_0^2 / F_s$  is the ratio of the reference inertia force associated with the fluid to that associated with the structural hinge,  $\rho_0$  the reference density,  $U_0$  the reference velocity,  $L_0$  the reference length,  $\tilde{m} = m / (\rho_0 L_0^3)$  the dimensionless bead mass,  $\tilde{U} = U / U_0$ , and  $\tilde{t} = t U_0 / L_0$ . The reference velocity  $U_0$  could for instance be the terminal velocity of the drop sedimenting in the air. Three dimensionless terms appear in Equation 3.3. The first term preceding the bead acceleration can conveniently be re-written as  $K = (\rho_0 U_0^2 L_0^2 / F_c) \times (F_c / F_s) = We \times Ec$ , where  $We$  is the Weber number. There is only a limited number of works reporting the Weber numbers in self-folding applications. We cite here the work by Antkowiak et al. [58], who reported a Weber number between  $0.2 < We < 15$ . The dimensionless number  $K$  hence covers multiple orders of magnitude. In the following, we set  $K = 1$  not only for simplicity but also because of a much shorter simulation time. The second term  $16(n_b - 1)^2$  represents the hinge length in terms of

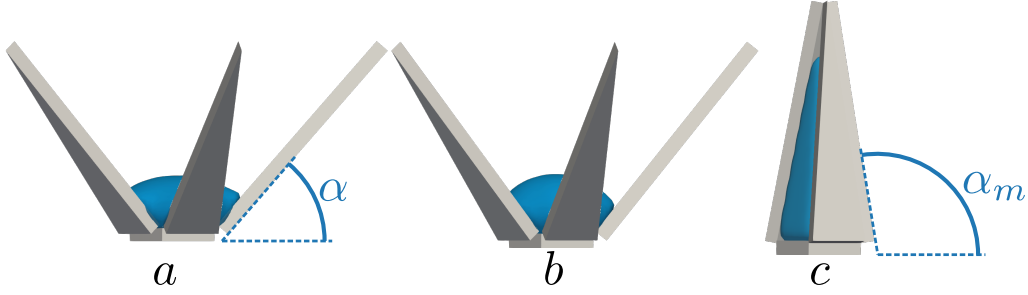


**Figure 9.** Partial folding and complete folding obtained at equilibrium. In a, the contact angle is set to  $\gamma = 70^\circ$  and, in b-c, it is set to  $\gamma = 90^\circ$ . The elasto-capillary number is set to  $Ec = 1.2$  in a-b and to  $Ec = 3.0$  in c. Because of the projection into a two-dimensional plane, only three side panels of the structural net are seen. In reality, there are  $N = 5$  side panels. The hinges are not shown.

bead number. The third term, that is  $L_c/R_d \sin(\gamma)Ec$ , represents the action of the surface tension force. Interestingly, the length of the three-phase contact line and the drop radius are in the same magnitude order, that is  $L_c/R_d \sim 1$ . In our simulations, the contact angle varies between  $70^\circ$  and  $90^\circ$ , meaning that  $\sin(\gamma) \sim 1$ . It turns out,  $Ec$  is the major contributor to the final equilibrium state. This is a strong advantage of the present normalization. To obtain fast and stable transient simulations, the bead mass along with the diagonal components of the moment of inertia matrix are set to  $\tilde{m} = 1$  and  $\tilde{I} = 1$ . Exact values for the bead mass and moment of inertia are only relevant for transient simulations, which are not of primary interest here. The response time related to the material damping is set to  $\tau_b L_0/U_0 = 0.05$ , thereby ensuring overdamped structural dynamics and hence further shortening the simulation time.

The non-dimensionalization also applies to the drop Equation 2.12, which reads

$$\frac{\partial \phi}{\partial \tilde{t}} + \frac{1}{Pe} \tilde{\mathbf{u}} \cdot \tilde{\nabla} \phi = -\frac{\delta \tilde{E}}{\delta \phi}, \quad (3.4)$$

where  $Pe = \tau_d U_0/L_0$  is the Peclet number,  $\tilde{\nabla} = \nabla/L_0$  and  $\tilde{\mathbf{u}} = \mathbf{u}/U_0$ . In most three-phase flow simulations, the Peclet number is chosen to be close to unity for stability reasons [59,60]. We do the same here and set  $Pe = 1$ . We stress, that  $K$  and  $Pe$  play a secondary role and only affect the transient folding dynamics. They do not affect the final steady-state configuration. One primary interest lies here in determining the critical elasto-capillary number  $\tilde{Ec}_c$ , at which the transition from partial to full drop encapsulation occurs. Setting  $K$  and  $Pe$  to unity has another advantage. It allows to adequately discretize Equations 3.3 and 3.4 with the same time step  $\delta t$ .

### (c) Folding

To quantitatively discuss the results, we further describe the folding angle  $\alpha$  between the base and the side panel. It is illustrated in Figure 9. The subscript in  $\alpha_m$  denotes the maximum folding angle, which corresponds to full drop encapsulation, that is when the shortest distance between two adjacent sides drops to zero. Figure 10 illustrates the folding angle as a function of time for the structural net with a five-sided base. The time abscissa is made non-dimensional with the denominator  $t_0 = 25L_0/U_0$ . At time  $t/t_0 = 0$ , the folding angle is zero. Irrespective of the elasto-capillary number, the folding angle smoothly increases until it reaches an equilibrium  $\alpha(t \rightarrow \infty) = \alpha_\infty$ . We select the data obtained with an elasto-capillary number ranging from  $Ec = 0.8$  to  $2.4$ . With  $Ec = 0.8$  and  $1.6$ , the encapsulation is only partial and the equilibrium folding angle equals  $\alpha_\infty = 31.6^\circ$  and  $67.2^\circ$ , respectively. With  $Ec = 2.4$ , a full encapsulation occurs and the folding angle is eventually capped by its maximum, which here equals  $\alpha_m = 98.7^\circ$ . In theory, that is when the gap is null, the maximum folding angle is  $\pi - \tan^{-1}(h/a)$ . For  $N = 3$

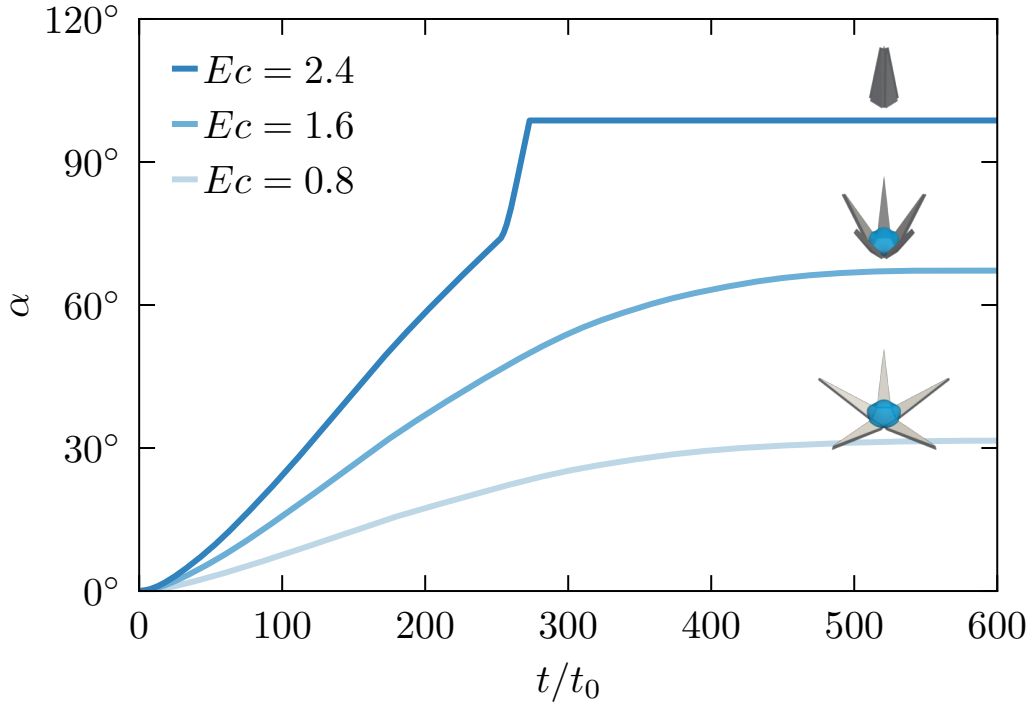


**Figure 10.** Folding angle ( $\alpha$ ) as a function of time. The base of the structural net is a pentagon, that is  $N = 5$ . The contact angle is set to  $\gamma = 70^\circ$ .  $Ec$  is the elasto-capillary number.

and  $N = 7$ , the maximum theoretical folding angle is  $97.3^\circ$  and  $98.1^\circ$ . A further strength of the model lies in the fact, that a transient investigation of the folding in terms of force balance is possible. At submillimetric scale and especially during the transient, force measurement remains an experimentally difficult task to perform. With our model, the surface tension force can be precisely determined as a function of the folding angle  $\alpha$ . This is shown in Figure 11 for  $\theta = 70^\circ$  and  $Ec = 1.5$ . With a number of side panels equal to  $N = 3$  and 4, full encapsulation occurs. With  $N = 3$ , that is the darkest blue curve, we show the three-phase contact line at selected positions in Figure 11a-f. The surface tension force initially increases linearly from position 'a' to 'b'. From position 'b' to 'd', the length of the three-phase contact line decreases and so, the surface tension force decreases too (Figure 11b-c). From position 'd' onwards, a second three-phase contact line near base of the triangular side panel appears (Figure 11d-e). The surface tension forces increases rapidly and full encapsulation occurs soon after. Figure 11f, shows the final three-phase contact line. With increasing number of side panels, see the light blue curves associated with  $N = 4$  to 7, the encapsulation is only partial and so, the surface tension force linearly decreases with  $\alpha$  to eventually stop at the steady-state abscissa  $\alpha_\infty = 38.7^\circ$ ,  $48.3^\circ$  and  $62.7^\circ$ , respectively.

The results, shown in Figures 10-11, suggest the existence of a critical elasto-capillary number, at which the transition from partial to full drop encapsulation occurs. To determine this transition, the equilibrium folding angle  $\alpha_\infty$  obtained for increasing  $Ec$  is shown in Figure 12. Irrespective of the number of side panels  $N$ , the equilibrium folding angle increases until it reaches its maximum capping value  $\alpha_m$ . To determine the transition from partial to full encapsulation, we approximate with a quadratic function of the form  $\tilde{\alpha}_\infty = \alpha_0 Ec + \alpha_1 Ec^2$  the data points satisfying  $\alpha_\infty < \alpha_m$ . The coefficients  $\alpha_0$  and  $\alpha_1$  are determined with a best-fit algorithm based on the least square method. The solution to the equation,  $\tilde{\alpha}_\infty(Ec) = \alpha_m$ , is then used to determine the critical elasto-capillary number  $\tilde{Ec}$ . An annotation illustrating the transitional abscissa  $\tilde{Ec}$  is shown in Figure 12.

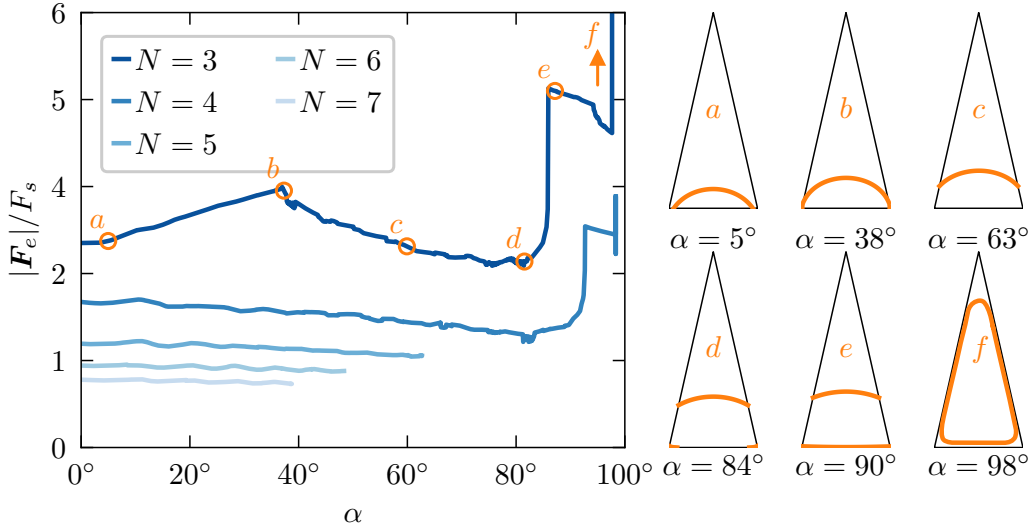


**Figure 11.** Surface tension force against folding angle  $\alpha$ . Data are obtained with  $\theta = 70^\circ$  and  $Ec = 1.5$ . The three-phase contact line is shown at selected positions, labelled a-f.  $\theta$  is the contact angle,  $Ec$  the elasto-capillary number,  $F_s$  the reference structural force and  $N$  the number of side panels in the structural net.

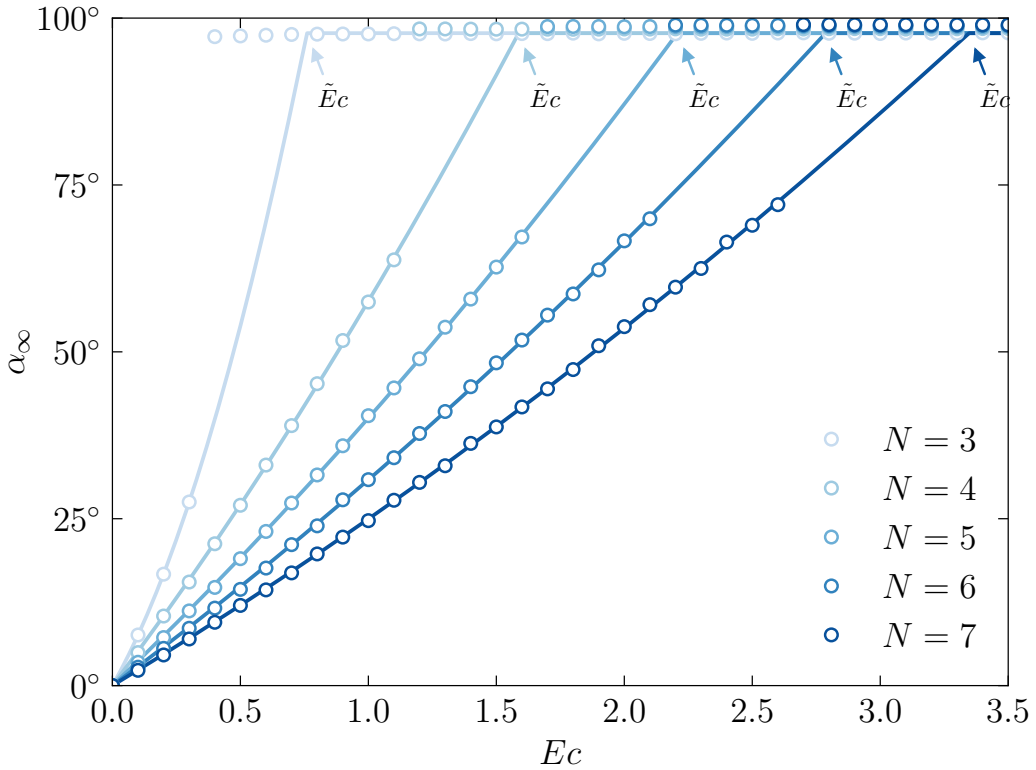


**Figure 12.** Equilibrium folding angle  $\alpha_\infty = \alpha(t \rightarrow \infty)$  against elasto-capillary number  $Ec$ . The data are shown for the contact angle  $\theta = 70^\circ$ .  $\tilde{Ec}$  is the critical value, at which full encapsulation occurs. The quadratic curves  $\tilde{\alpha}_\infty(Ec)$  are best fitted to the simulation data.  $N$  is the number of side panels.



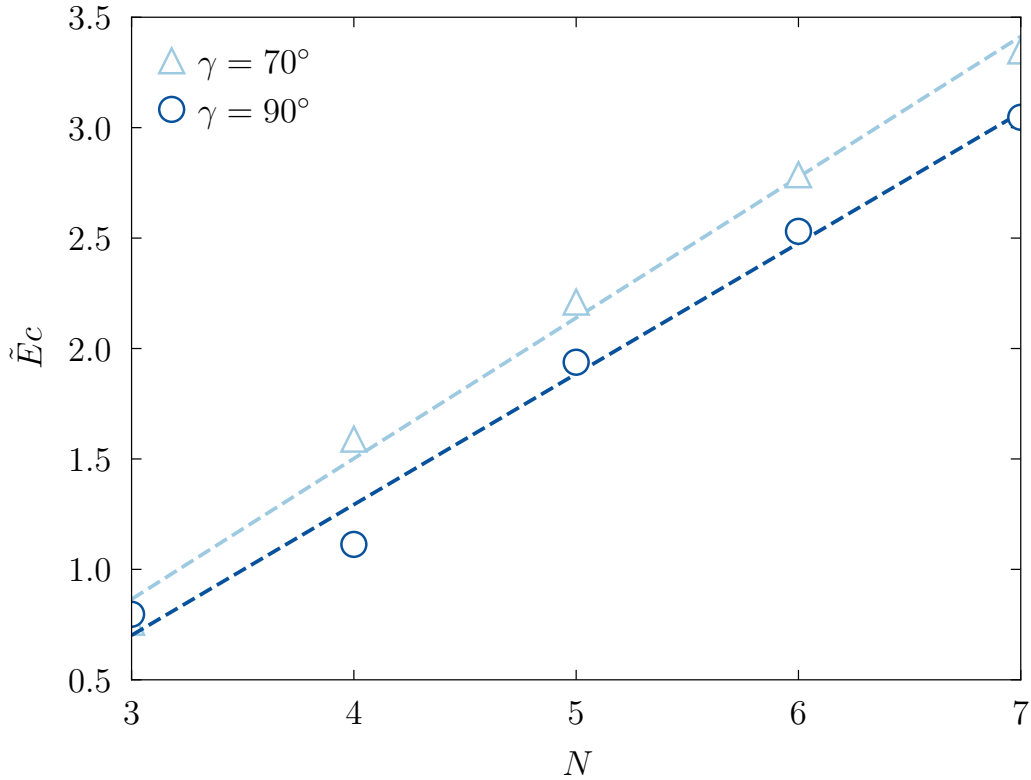


**Figure 13.** Critical elasto-capillary number  $\tilde{E}c$ , at which full drop encapsulation occurs. The dashed lines are a guide for the eye and aim at showing the linear dependency with the number of side panels.

An increase in the number of panels results in a greater critical number  $\tilde{E}c$ . According to Equation 2.2, this is to be expected. With increasing  $N$ , the side panels become narrower, that is  $s$  decreases. This in-turn leads to a shorter contact line and hence to a lower surface tension force driving the folding process. To better illustrate this trend, the critical elasto-capillary number is shown in Figure 13 against the number of side panels  $N$  for the contact angles  $\gamma = 70^\circ$  and  $90^\circ$ . It is found, that the critical elasto-capillary follows a linear trend with increasing number of triangular side panels  $N$  in the structural net. We also find, that a lower contact angle, that is a drop with higher affinity to the structural net, does not necessarily trigger encapsulation at lower  $\tilde{E}c$ . With a stronger affinity to the structural net, the drop extends on the thin extruded sides and so, the normal component of the surface tension force is reduced.

## 4. Conclusions

We have introduced a numerical framework that combines structural and surface-energy minimization models to simulate complex nano- and micro-origami self-folding processes in three dimensions. Our model involves a liquid drop that induces spontaneous folding and dynamic deformation of the structural net. As application, we have simulated the self-folding of two-dimensional templates into pyramidal micro-structures and determined the transition from partial to full drop encapsulation. We here varied the number of triangular side panels along with the elasto-capillary number. A more advanced parameter study could have been performed. For instance, we tried to investigate the change in a hinge length  $\ell$  as well. With a good affinity to the solid, that is  $\gamma < 80^\circ$ , and a panel gap greater than a few grid size elements, the liquid

slowly diffused to the other side of the structural net. Such simulations were hence not included. Advantages of the model include the incorporation of time-derivative terms addressing unsteady three-dimensional dynamics. In the future, the model will be extended to consider more arbitrary structural nets, for example with an asymmetry. Evaporation will also be considered, because in the submillimeter scale, it can occur rapidly. This can be done in a relatively easy way by changing the tuning the parameter  $\beta$  in Equation 2.14.

## Acknowledgments

This work was supported by the German Research Foundation (Deutsche Forschungsgemeinschaft) under the project numbers 492454247 and 419981939.

## Funding

This work was supported by the German Research Foundation (Deutsche Forschungsgemeinschaft) under the project numbers 492454247 and 419981939.

## References

1. Py C, Reverdy P, Doppler L, Bico J, Roman B, Baroud CN. 2007 Capillary origami: spontaneous wrapping of a droplet with an elastic sheet. *Physical Review Letters* **98**, 156103. ([10.1103/PhysRevLett.98.156103](https://doi.org/10.1103/PhysRevLett.98.156103))
2. Roman B, Bico J. 2010 Elasto-capillarity: deforming an elastic structure with a liquid droplet. *Journal of Physics: Condensed Matter* **22**, 493101. ([10.1088/0953-8984/22/49/493101](https://doi.org/10.1088/0953-8984/22/49/493101))
3. Bae J, Ouchi T, Hayward RC. 2015 Measuring the elastic modulus of thin polymer sheets by elastocapillary bending. *ACS Applied Materials & Interfaces* **7**, 14734–14742. ([10.1021/acsami.5b02567](https://doi.org/10.1021/acsami.5b02567))
4. Bico J, Reyssat É, Roman B. 2018 Elastocapillarity: when surface tension deforms elastic solids. *Annual Review of Fluid Mechanics* **50**, 629–659. ([10.1146/annurev-fluid-122316-050130](https://doi.org/10.1146/annurev-fluid-122316-050130))
5. Kwok KS, Huang Q, Mastrangeli M, Gracias DH. 2020 Self-folding using capillary forces. *Advanced Materials Interfaces* **7**, 1901677. ([10.1002/admi.201901677](https://doi.org/10.1002/admi.201901677))
6. Reis PM, Hure J, Jung S, Bush JWM, Clanet C. 2010 Grabbing water. *Soft Matter* **6**, 5705–5708. ([10.1039/C0SM00895H](https://doi.org/10.1039/C0SM00895H))
7. Syms R, Yeatman E, Bright V, Whitesides G. 2003 Surface tension-powered self-assembly of microstructures – the state-of-the-art. *Journal of Microelectromechanical Systems* **12**, 387–417. ([10.1109/JMEMS.2003.811724](https://doi.org/10.1109/JMEMS.2003.811724))
8. Guo X, Li H, Ahn BY, Duoss EB, Hsia KJ, Lewis JA, Nuzzo RG. 2009 Two- and three-dimensional folding of thin film single-crystalline silicon for photovoltaic power applications. *Proceedings of the National Academy of Sciences* **106**, 20149–20154. ([10.1073/pnas.0907390106](https://doi.org/10.1073/pnas.0907390106))
9. Zhang Y, Zhang F, Yan Z, Ma Q, Li X, Huang Y, Rogers JA. 2017 Printing, folding and assembly methods for forming 3D mesostructures in advanced materials. *Nature Reviews Materials* **2**, 17019. ([10.1038/natrevmats.2017.19](https://doi.org/10.1038/natrevmats.2017.19))
10. Lorenz P, Franz R, Ehrhardt M, Lecrivain G, Kirchner R, Zimmer K. 2023 Laser cutting of polymer templates for water-droplet induced self-folding of cubes: hinge geometry optimization. *Journal of Laser Micro Nanoengineering* **18**. ([10.2961/jlmn.2023.02.2001](https://doi.org/10.2961/jlmn.2023.02.2001))
11. Demaine ED, O'Rourke J. 2007 *Geometric folding algorithms: linkages, origami, polyhedra*. Cambridge University Press. ([10.1017/CBO9780511735172](https://doi.org/10.1017/CBO9780511735172))
12. Pandey S, Ewing M, Kunas A, Nguyen N, Gracias DH, Menon G. 2011 Algorithmic design of self-folding polyhedra. *Proceedings of the National Academy of Sciences* **108**, 19885–19890. ([10.1073/pnas.111085710](https://doi.org/10.1073/pnas.111085710))
13. Kaplan R, Klobusicky J, Pandey S, Gracias DH, Menon G. 2014 Building polyhedra by self-assembly: theory and experiment. *Artificial Life* **20**, 409–439.
14. Twohig T, Croll AB. 2021 Adhesion directed capillary origami. *Soft Matter* **17**, 9170–9180. ([10.1039/D1SM01142A](https://doi.org/10.1039/D1SM01142A))
15. Ionov L. 2011 Soft microorigami: self-folding polymer films. *Soft Matter* **7**, 6786–6791. ([10.1039/C1SM05476G](https://doi.org/10.1039/C1SM05476G))

16. Fernandes R, Gracias DH. 2012 Self-folding polymeric containers for encapsulation and delivery of drugs. *Advanced Drug Delivery Reviews* **64**, 1579–1589. Emerging micro- and nanotechnologies for the development of novel drug delivery devices and systems ([10.1016/j.addr.2012.02.012](https://doi.org/10.1016/j.addr.2012.02.012))
17. Bolanos Quinones VA, Zhu H, Solovev AA, Mei Y, Gracias DH. 2018 Origami biosystems: 3D assembly methods for biomedical applications. *Advanced Biosystems* **2**, 1800230. ([10.1002/adbi.201800230](https://doi.org/10.1002/adbi.201800230))
18. Patra N, Wang B, Král P. 2009 Nanodroplet activated and guided folding of graphene nanostructures. *Nano Letters* **9**, 3766–3771. PMID: 19852466 ([10.1021/nl9019616](https://doi.org/10.1021/nl9019616))
19. Liu Q, Xu B. 2018 Two- and three-dimensional self-folding of free-standing graphene by liquid evaporation. *Soft Matter* **14**, 5968–5976. ([10.1039/C8SM00873F](https://doi.org/10.1039/C8SM00873F))
20. Brakke KA. 1992 The Surface Evolver. *Experimental Mathematics* **1**, 141–165. ([10.1080/10586458.1992.10504253](https://doi.org/10.1080/10586458.1992.10504253))
21. Leong TG, Lester PA, Koh TL, Call EK, Gracias DH. 2007 Surface tension-driven self-folding polyhedra. *Langmuir* **23**, 8747–8751. PMID: 17608507 ([10.1021/la700913m](https://doi.org/10.1021/la700913m))
22. van Honschoten JW, Berenschot JW, Ondarçuhu T, Sanders RGP, Sundaram J, Elwenspoek M, Tas NR. 2010 Elastocapillary fabrication of three-dimensional microstructures. *Applied Physics Letters* **97**, 014103. ([10.1063/1.3462302](https://doi.org/10.1063/1.3462302))
23. Legrain A, Janson TG, Berenschot JW, Abelman L, Tas NR. 2014 Controllable elastocapillary folding of three-dimensional micro-objects by through-wafer filling. *Journal of Applied Physics* **115**, 214905. ([10.1063/1.4878460](https://doi.org/10.1063/1.4878460))
24. de Langre E, Baroud C, Reverdy P. 2010 Energy criteria for elasto-capillary wrapping. *Journal of Fluids and Structures* **26**, 205–217. ([10.1016/j.jfluidstructs.2009.10.004](https://doi.org/10.1016/j.jfluidstructs.2009.10.004))
25. Brubaker N, Lega J. 2016a Two-dimensional capillary origami. *Physics Letters A* **380**, 83–87. ([10.1016/j.physleta.2015.09.002](https://doi.org/10.1016/j.physleta.2015.09.002))
26. Brubaker ND, Lega J. 2016b Capillary-induced deformations of a thin elastic sheet. *Philosophical Transactions of the Royal Society A: Mathematical, Physical and Engineering Sciences* **374**, 20150169. ([10.1098/rsta.2015.0169](https://doi.org/10.1098/rsta.2015.0169))
27. Neukirch S, Antkowiak A, Marigo JJ. 2013 The bending of an elastic beam by a liquid drop: a variational approach. *Proceedings of the Royal Society A: Mathematical, Physical and Engineering Sciences* **469**, 20130066. ([10.1098/rspa.2013.0066](https://doi.org/10.1098/rspa.2013.0066))
28. Bosi F, Misseroni D, Dal Corso F, Bigoni D. 2015 Self-encapsulation, or the ‘dripping’ of an elastic rod. *Proceedings of the Royal Society A: Mathematical, Physical and Engineering Sciences* **471**, 20150195. ([10.1098/rspa.2015.0195](https://doi.org/10.1098/rspa.2015.0195))
29. Joshi SY, Deshmukh SA. 2021 A review of advancements in coarse-grained molecular dynamics simulations. *Molecular Simulation* **47**, 786–803. ([10.1080/08927022.2020.1828583](https://doi.org/10.1080/08927022.2020.1828583))
30. Elettro H, Grandgeorge P, Neukirch S. 2017 Elastocapillary coiling of an elastic rod inside a drop. *Journal of Elasticity* **127**, 235–247. ([10.1007/s10659-016-9611-4](https://doi.org/10.1007/s10659-016-9611-4))
31. Aihara S, Takaki T, Takada N. 2019 Multi-phase-field modeling using a conservative Allen–Cahn equation for multiphase flow. *Computers & Fluids* **178**, 141–151. ([10.1016/j.compfluid.2018.08.023](https://doi.org/10.1016/j.compfluid.2018.08.023))
32. Jacobson A, Panozzo D et al.. 2018 libigl: A simple C++ geometry processing library. <https://libigl.github.io/>.
33. Lorensen WE, Cline HE. 1987 Marching cubes: A high resolution 3D surface construction algorithm. *SIGGRAPH Comput. Graph.* **21**, 163–169. ([10.1145/37402.37422](https://doi.org/10.1145/37402.37422))
34. André D, Iordanoff I, Charles JL, Néauport J. 2012 Discrete element method to simulate continuous material by using the cohesive beam model. *Computer Methods in Applied Mechanics and Engineering* **213–216**, 113–125. ([10.1016/j.cma.2011.12.002](https://doi.org/10.1016/j.cma.2011.12.002))
35. Fertis D. 1993 *Nonlinear mechanics*. Taylor & Francis.
36. Lecrivain G, Grein TBP, Yamamoto R, Hampel U, Taniguchi T. 2020 Eulerian/Lagrangian formulation for the elasto-capillary deformation of a flexible fibre. *Journal of Computational Physics* **409**, 109324. ([10.1016/j.jcp.2020.109324](https://doi.org/10.1016/j.jcp.2020.109324))
37. Guo Y, Wassgren C, Curtis JS, Xu D. 2018 A bonded sphero-cylinder model for the discrete element simulation of elasto-plastic fibers. *Chemical Engineering Science* **175**, 118–129. ([10.1016/j.ces.2017.09.029](https://doi.org/10.1016/j.ces.2017.09.029))
38. Banerjee A, Bhattacharya B, Mallik A. 2008 Large deflection of cantilever beams with geometric non-linearity: Analytical and numerical approaches. *International Journal of Non-Linear Mechanics* **43**, 366–376. ([10.1016/j.ijnonlinmec.2007.12.020](https://doi.org/10.1016/j.ijnonlinmec.2007.12.020))

39. Ruocco E, Reddy J. 2023 Analytical solutions of Reddy, Timoshenko and Bernoulli beam models: A comparative analysis. *European Journal of Mechanics - A/Solids* **99**, 104953. ([10.1016/j.euromechsol.2023.104953](https://doi.org/10.1016/j.euromechsol.2023.104953))
40. Araki T, Tanaka H. 2006 Wetting-induced depletion interaction between particles in a phase-separating liquid mixture. *Physical Review E* **73**, 061506. ([10.1103/PhysRevE.73.061506](https://doi.org/10.1103/PhysRevE.73.061506))
41. Lecrivain G, Kotani Y, Yamamoto R, Hampel U, Taniguchi T. 2018 Diffuse interface model to simulate the rise of a fluid droplet across a cloud of particles. *Phys. Rev. Fluids* **3**, 094002. ([10.1103/PhysRevFluids.3.094002](https://doi.org/10.1103/PhysRevFluids.3.094002))
42. Nonomura M. 2012 Study on Multicellular Systems Using a Phase Field Model. *PLOS ONE* **7**, 1–9. ([10.1371/journal.pone.0033501](https://doi.org/10.1371/journal.pone.0033501))
43. Lavoratti TC, Heitkam S, Hampel U, Lecrivain G. 2021 A computational method to simulate mono- and poly-disperse two-dimensional foams flowing in obstructed channel. *Rheologica Acta* **60**, 587–601. ([10.1007/s00397-021-01288-y](https://doi.org/10.1007/s00397-021-01288-y))
44. Lee HG, Kim J. 2008 A second-order accurate non-linear difference scheme for the N - component Cahn–Hilliard system. *Physica A: Statistical Mechanics and its Applications* **387**, 4787–4799. ([10.1016/j.physa.2008.03.023](https://doi.org/10.1016/j.physa.2008.03.023))
45. Boyer F, Lapuerta C, Minjeaud S, Piar B, Quintard M. 2010 Cahn–Hilliard/Navier–Stokes model for the simulation of three-phase flows. *Transport in Porous Media* **82**, 463–483. ([10.1007/s11242-009-9408-z](https://doi.org/10.1007/s11242-009-9408-z))
46. Yang J, Kim J. 2020 A phase-field method for two-phase fluid flow in arbitrary domains. *Computers & Mathematics with Applications* **79**, 1857–1874. ([10.1016/j.camwa.2019.10.008](https://doi.org/10.1016/j.camwa.2019.10.008))
47. Baerentzen J, Aanaes H. 2005 Signed distance computation using the angle weighted pseudonormal. *IEEE Transactions on Visualization and Computer Graphics* **11**, 243–253. ([10.1109/TVCG.2005.49](https://doi.org/10.1109/TVCG.2005.49))
48. Shinto H, Miyahara M, Higashitani K. 1999 Evaluation of interaction forces between macroparticles in simple fluids by molecular dynamics simulation. *Journal of Colloid and Interface Science* **209**, 79–85. ([10.1006/jcis.1998.5870](https://doi.org/10.1006/jcis.1998.5870))
49. Brackbill J, Kothe D, Zemach C. 1992 A continuum method for modeling surface tension. *Journal of Computational Physics* **100**, 335–354. ([10.1016/0021-9991\(92\)90240-Y](https://doi.org/10.1016/0021-9991(92)90240-Y))
50. Kim J. 2005 A continuous surface tension force formulation for diffuse-interface models. *Journal of Computational Physics* **204**, 784–804. ([10.1016/j.jcp.2004.10.032](https://doi.org/10.1016/j.jcp.2004.10.032))
51. Dierckx P. 1993 *Curve and surface fitting with splines*. Oxford University Press.
52. Balay S, Abhyankar S, Adams MF, Benson S, Brown J, Brune P, Buschelman K, Constantinescu EM, Dalcin L, Dener A, Eijkhout V, Groppe WD, Hapla V, Isaac T, Jolivet P, Karpeev D, Kaushik D, Knepley MG, Kong F, Kruger S, May DA, McInnes LC, Mills RT, Mitchell L, Munson T, Roman JE, Rupp K, Sanan P, Sarich J, Smith BF, Zampini S, Zhang H, Zhang H, Zhang J. 2022 PETSc Web page. <https://petsc.org/>.
53. Dierckx P. 1993 FITPACK. <https://netlib.org/dierckx/>.
54. Lecrivain G. 2024 Self-folding of two-dimensional thin templates into pyramidal microstructures by a liquid drop - a numerical model. <https://rodare.hzdr.de/deposit/2803>. ([10.14278/rodare.2803](https://doi.org/10.14278/rodare.2803))
55. Hu H, Larson RG. 2002 Evaporation of a sessile droplet on a substrate. *The Journal of Physical Chemistry B* **106**, 1334–1344. ([10.1021/jp0118322](https://doi.org/10.1021/jp0118322))
56. Schmieschek S, Harting J. 2011 Contact angle determination in multicomponent lattice Boltzmann simulations. *Communications in Computational Physics* **9**, 1165–1178. ([10.4208/cicp.201009.271010s](https://doi.org/10.4208/cicp.201009.271010s))
57. Si H. 2015 TetGen, a Delaunay-based quality tetrahedral mesh generator. *ACM Transactions on Mathematical Software* **41**, 1–36. ([10.1145/2629697](https://doi.org/10.1145/2629697))
58. Antkowiak A, Audoly B, Josserand C, Neukirch S, Rivetti M. 2011 Instant fabrication and selection of folded structures using drop impact. *Proceedings of the National Academy of Sciences* **108**, 10400–10404. ([10.1073/pnas.1101738108](https://doi.org/10.1073/pnas.1101738108))
59. Sun X, Sakai M. 2016 Numerical simulation of two-phase flows in complex geometries by using the volume-of-fluid/immersed-boundary method. *Chemical Engineering Science* **139**, 221–240. ([10.1016/j.ces.2015.09.031](https://doi.org/10.1016/j.ces.2015.09.031))
60. Nath G, Ray B. 2021 Manipulating the three-phase contact line of an evaporating particle-laden droplet to get desirable microstructures: A lattice Boltzmann study. *Physics of Fluids* **33**, 083304. ([10.1063/5.0052878](https://doi.org/10.1063/5.0052878))

## Ethics statement

This article did not involve human participants or animals.

## Competing interests statement

The authors report no conflict of interest.

## Data accessibility statement

The source code and the data that support the findings of this study has been made available with a DOI number. The link is given in the bibliography [54].

## Author contributions

GL developed the model, performed the simulation and wrote the first draft of the manuscript. PL and KZ performed the illustrative experiment. GL, KZ and UH contributed to the acquisition of the financial support for this work. All authors aided in interpreting the results and work on the manuscript.